

## Direct methanol fuel cell (DMFC): analysis of residence time behaviour of anodic flow bed

U. Krewer<sup>a</sup>, Y. Song<sup>a</sup>, K. Sundmacher<sup>a,\*</sup>, V. John<sup>b</sup>, R. Lübke<sup>b</sup>, G. Matthies<sup>b,c</sup>, L. Tobiska<sup>b</sup>

<sup>a</sup>Max-Planck-Institut (MPI) für Dynamik Komplexer Technischer Systeme, Sandtorstrasse 1, 39106 Magdeburg, Germany

<sup>b</sup>Institut für Analysis und Numerik, Otto-von-Guericke-Universität Magdeburg, Postfach 4120, 39016 Magdeburg, Germany

<sup>c</sup>Ruhr-Universität, Bochum Fakultät für Mathematik, Universitätsstrasse 150, 44780 Bochum, Germany

Received 2 June 2003; received in revised form 25 August 2003; accepted 23 September 2003

### Abstract

This paper studies the residence time behaviour and concentration distribution in a simplified rhomboidal DMFC anode flow bed by 3D numerical flow simulations and by experimental measurements. The rhomboidal DMFC anode flow bed and the applied volume flow are discussed with regard to data given in the literature. Simulations with CFX, based on Finite Volume Method, and MoonMD, based on Finite Element Method, show strongly similar results and the reliability of the computed residence time distributions (RTD) is proved by showing that they depend only slightly on parameters of the numerical schemes applied. The realisation of the RTD and concentration distribution measurements are described. Experimentally obtained RTD results are in good agreement with the numerical simulations. Also, the experimentally obtained concentration distribution inside the anode flow bed is very similar to the computed distribution. By analysing the RTDs and concentration distributions, the obtained results provided evidence of weaknesses of the flow bed design.

© 2003 Elsevier Ltd. All rights reserved.

**Keywords:** Flow bed design; Fuel distribution; Transient response; Dynamic simulation; Mass transfer; CFD

### 1. Introduction

The direct methanol fuel cell (DMFC) is a potential power source in mobile and stationary applications. It offers several advantages in comparison to hydrogen fed polymer electrolyte membrane fuel cells (PEMFC), e.g. since the fuel is an aqueous-based methanol solution, it can be processed and stored easier than gases. Recent publications give a good overview of the current state of the art in the development of DMFCs (Arico et al., 2001; Schultz et al., 2001). Together with these advantages, the DMFC shows significantly lower power densities than PEMFCs, due to slow methanol oxidation kinetics and mass transport problems, i.e. transport of carbon dioxide out of the system and methanol crossover through the membrane to the cathode side.

Besides intense studies of the methanol crossover (Heinzel and Barragan, 1999), several research teams investigated the anode flow characteristics, e.g. by

volume flow variation (Scott et al., 1999c), carbon dioxide monitoring (Argyropoulos et al., 1999a) or flow bed characterisation.

Various flow bed designs for liquid DMFCs are reported in the literature, e.g. parallel channel designs (Amphlett et al., 2001; Argyropoulos et al., 1999a,b; Scott et al., 1998, 1999c), parallel channel designs with triangular inlet and outlet zones (Argyropoulos et al., 1999a,b; Scott et al., 1999a), spot designs (Gulzow et al., 2002; Scott et al., 1998), meander designs (Geiger et al., 2000) and mesh designs (Scott et al., 2001). Arico et al. (2000) recently investigated an optimal flow bed design for vapour fed DMFCs. They ascribed to flow bed design a non-negligible effect on mass transfer characteristics, and as a result on methanol crossover. Several studies compare different compartment designs with respect to their influence on the electrochemical cell performance, on the carbon dioxide transport and with regard to practical considerations: Amphlett et al. (2001) showed for a parallel channel design that the channel depth directly influences the cell performance. Scott and colleagues (Argyropoulos et al., 1999a; Scott et al., 1998, 1999a) examined various flow beds designs and their effect on the carbon dioxide transport. Furthermore,

\* Corresponding author. Tel.: +49-391-6110-350;  
fax: +49-391-6110-353.

E-mail address: sundmacher@mpi-magdeburg.mpg.de  
(K. Sundmacher).

Scott et al. (2001) compared stainless steel mesh flow beds of different mesh sizes with parallel and spot designs, respectively, indicating that mesh designs may be a cost-reducing alternative. The same authors discussed gains and drawbacks of the spot design (Scott et al., 1998). Further publications from this group present a parallel channel design with triangular inlet and outlet zones, based on a heat exchanger design concept. It showed a more uniform flow than the simple parallel channel design (Argyropoulos et al., 1999a; Scott et al., 1999a). It can be summarised that the criteria for an optimal flow bed are manifold. The design performance depends on operating conditions like temperature and pressure, which determine the state of the fluid and hence also carbon dioxide transport phenomena. As a result, an optimal design should only be defined for respective operating conditions.

Computational fluid dynamics (CFD) techniques have been proved to be a powerful approach to study the complex flow and transport phenomena in fuel cells. Besides the low costs of the numerical modelling, CFD has additional advantages: analysis of the flow field in a fuel cell by this method can be used easily for different anode compartments. A lot of research work has been done by means of CFD to simulate different fuel cells, for example phosphotungstic acid fuel cells (PWAFC) (Lavric et al., 2001), molten carbonate fuel cells (MCFC) (He and Chen, 1998) and PEMFCs (Dutta et al., 2000). Baxter et al. (1999) developed a one-dimensional mathematical model for a liquid fed DMFC. Wang et al. (1996) discussed the effects of the anode catalyst layer structure on the cell performance. Kulikovskiy et al. (2000) studied numerically a vapour-fed DMFC with a two-dimensional model and a new designed current collector was developed based on the analysis of the detailed current density distributions in backing, catalyst layer and membrane.

The goal of this paper is to investigate the performance of a liquid fed rhomboidal DMFC anode compartment. The research has been focused on the residence time distribution (RTD) and the concentration distribution inside the compartment. Investigations are made in two ways, by experimental measurements and by 3D numerical simulations. To the authors knowledge up to now no such investigations on fuel cells, either by experimental or by computational means, are found in literature, although it is indeed very helpful for the characterisation and improvement of the dynamic behaviour of fuel cells. The anode compartment and the realisation of the RTD measurements are described in Section 2. The main features of the anode compartment are an active area placed on parallel channels, and spotted triangular inlet and outlet zones. The RTD is studied by injecting a tracer into the anode compartment. The modelling part was done by computational fluid dynamics. The transport of the tracer is described by a time-dependent 3D convection–diffusion equation. The flow field is given by the solution of the Navier–Stokes equations. These equations are given in Section 3. That section describes also some features of the codes which were

used in the numerical simulations. One of them is CFX 4.4, a commercial software package which is based on the finite volume method. The other one, MooNMD, is a research code using the finite element method. The numerical studies are presented in Section 4 and compared to the experimentally gained RTD. In addition, the influence of several parameters of the numerical schemes on the simulated RTDs is studied. To obtain an insight in the evolution of the tracer distribution within the anode compartment of the fuel cell, snap shots of the experimental observation together with corresponding snap shots from the numerical simulations are presented. The key results of this paper are summarised in Section 5.

## 2. Experimental investigations

### 2.1. Anode compartment

Based on the parallel channel design with triangular inlet and outlet zones, we developed the flow bed shown in Fig. 1. Its geometry is similar to the design by Scott and colleagues (Argyropoulos et al., 1999a; Scott et al., 1999a), which was reported to generate an enhanced uniform flow distribution and which we, therefore, consider as a good starting point for flow distribution studies. In contrast to their design, we strongly simplified the structure, so that the flow bed is suitable for basic studies on residence time behaviour and it is easy to implement the geometry into software and to simulate. The number of channels was reduced from ca. 60 to 6, and the channel width and depth was 2.5 times enlarged. Channel width, channel depth and rip width are now 5 mm. The triangular area at the inlet generates a more homogeneous flow distribution. It does not belong to the active electrode area, whose size is 22 cm<sup>2</sup>. In comparison with the literature design, the coarser distribution structure will worsen the distribution of reactant, and the thickness of the ribs lessens the active area usable for reaction. Nonetheless, the structure still bears the basic functionalities that characterise the design of Scott and colleagues. In the following we will denote this simplified parallel flow bed design with triangular in- and outlet zones as ‘(simplified) rhomboidal design’ due to its outer shape.

In the studies of Scott and colleagues, a frequently used volume flow with the improved parallel channel design is 1.36 ml/min (Sundmacher et al., 2001; Sundmacher and Scott, 1999; Zhou et al., 2001). Using the geometry mentioned there, we receive a Reynolds number of  $Re = 1.32$  inside the channels. To establish realistic and comparable flow conditions in our cell’s active electrode area, a volume flow of 2 ml/min was calculated for the cell by using the same Reynolds number as above for the channels. A further measure to compare volume flows in anode compartments of DMFCs is the specific volume flow, i.e. volume flow per active area. This ratio indicates which volume

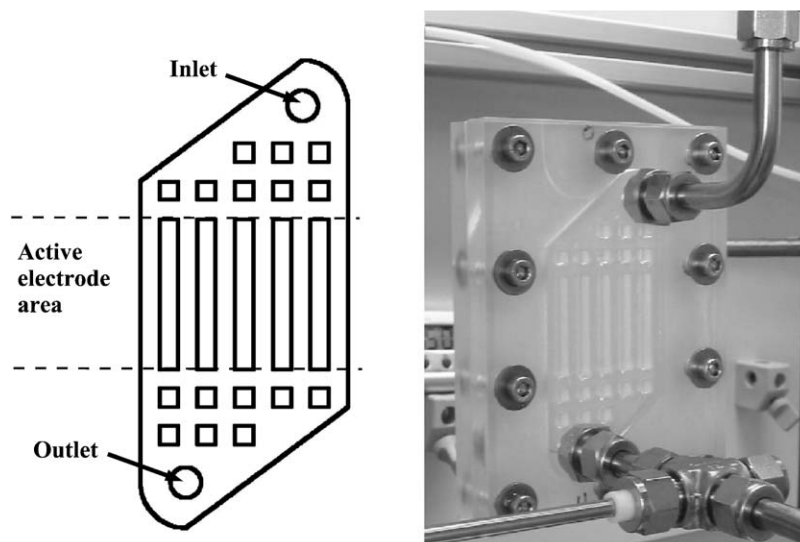


Fig. 1. Anodic compartment design (left) and its integration into the experimental setup (right).

Table 1  
Literature survey: volume flows per area for liquid fed DMFCs

| Source  | Volume flow (cm <sup>3</sup> /min) | Area (cm <sup>2</sup> ) | Specific volume flow (cm <sup>3</sup> /(cm <sup>2</sup> min)) |
|---|------------------------------------|-------------------------|---|
| Nordlund et al. (2002)                          | 0.3                                | 1                       | 0.3   |
| Wei et al. (2002)                               | 1                                  | 9                       | 0.11  |
| Hikita et al. (2002)                            | 5                                  | 25                      | 0.2   |
| Jorissen et al. (2002)                          | 4                                  | 25                      | 0.16  |
| Geiger et al. (2001)                            | 10                                 | 30                      | 0.33  |
| Scott et al. (1998)                             | 0.84–6.96                          | 9                       | 0.093–0.773   |
| Scott et al. (1999b)                            | 0.84, 1.36                         | 9                       | 0.093, 0.1511   |
| Sundmacher et al. (2001) and Zhou et al. (2001) | 1.36                               | 9                       | 0.1511  |
| Shukla et al. (2002)                            | 15                                 | 25                      | 0.6   |
| Gulzow et al. (2002)                            | 20                                 | 25                      | 0.8   |
| Sundmacher and Scott (1999)                     | 640                                | 100                     | 6.4   |

flow is necessary to deliver sufficient amount of methanol to the membrane electrode assembly. Table 1 gives a literature survey of these parameters. A suitable range for usual applications seems to be 0.1–0.3 cm<sup>3</sup>/(cm<sup>2</sup> min), which would indicate a volume flow of 2.2–6.6 cm<sup>3</sup>/min for the rhomboidal anode compartment. The result obtained via the Reynolds number,  $V_F = 2$  ml/min, lies next to this range and is subsequently used as the default volume flow.

Polyacrylics was chosen as manufacturing material. This enables the monitoring of the flow inside the cell.

## 2.2. Experimental setup

A setup according to Fig. 2 was constructed. Two pressure vessels, operating pressure 2 kPa abs., cause the driving

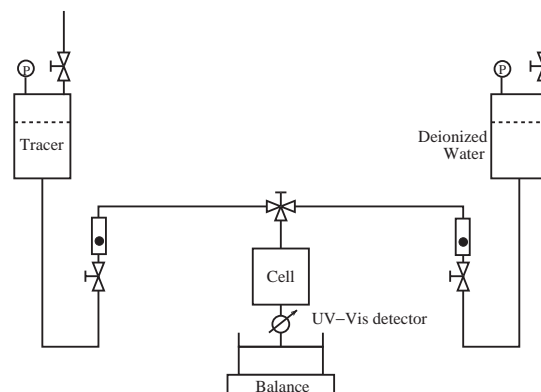


Fig. 2. Residence time measuring device.

force which moves the fluid through the cell. Hence, pulsation via pumps is avoided. The volume flow was adjusted via rotameter and additionally monitored via balance. The applied measuring technique was UV-Vis spectroscopy, equipment: Specord 50, Analytik Jena. The respective online testing probe was installed at the outlet of the cell. As a tracer substance, we selected eosin (Basacid Rot 316, BASF) with maximum absorption at a wavelength of  $\lambda_{\max} = 515$  nm. After recording a calibration curve at this wavelength, we fixed a concentration range from 0 to  $5.5 \times 10^{-6}$  mol/l in which the Lambert–Beer law is valid. Subsequently, a tracer concentration of  $5 \times 10^{-6}$  mol/l was used. Aging tests were conducted to verify that the solution is time stable within 3 h (maximum relative error = 3.68%). A three-way cock is used to switch from deionised water to eosin solution, causing the concentration step in front of the cell. To avoid disturbance in the velocity profile, the pipes connecting the cock with the cell, and the pipes connecting the cell with the online probe have the same diameter as the inlet and outlet of the cell. Since these pipes constitute 36.7 vol% of

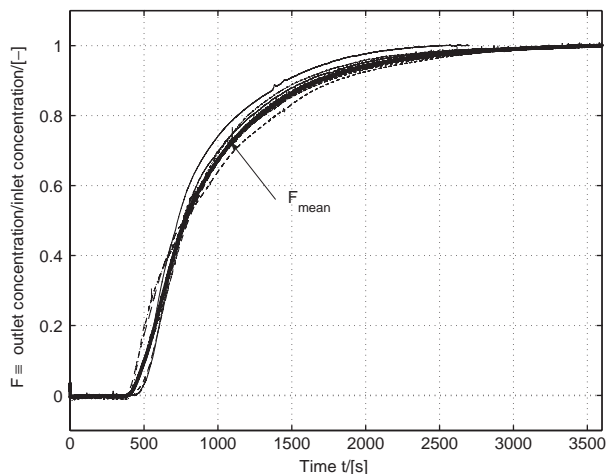


Fig. 3. Successively recorded RTDs and mean RTD for anode compartment plus inlet and outlet pipes.

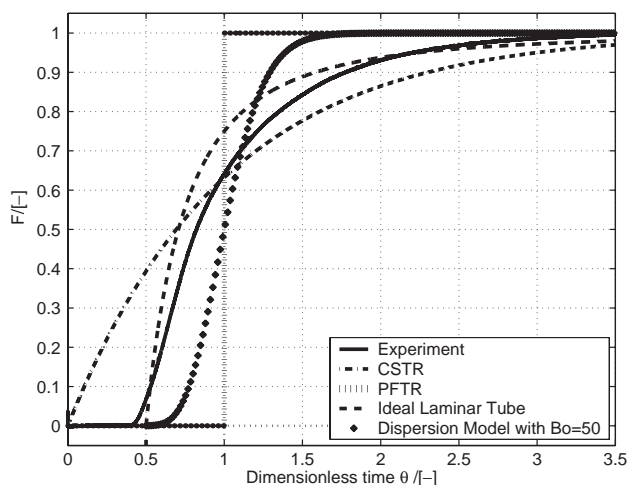


Fig. 4. Comparison of experimental RTD with ideal reactor RTDs.

the whole tested equipment, their influence is crucial for the results and the simulation. During the experiments, a video camera recorded the propagation of the tracer flow through the cell.

### 2.3. RTD measurements

RTD measurements were conducted for 60 min, see Fig. 3. The curve shows a stable behaviour and is largely reproducible. The first eosin molecules were detected at the outlet after 375 s, i.e. dimensionless time  $\theta = t/\tau = 0.39$ . The mean residence time  $\tau = V/V_F$ , i.e. the ratio of cell volume to volume flow, is 948 s ( $\theta = 1$ ), while 50% of the molecules inserted at  $t=0$  s have left the cell after  $t_{50}=781$  s ( $\theta = 0.82$ ).

Fig. 4 shows the experimental curve in comparison to the residence time of ideal reactors at the given volume and

volume flow: continuous stirred tank reactor (CSTR), plug flow tubular reactor (PFTR), ideal laminar flow tubular reactor (Poiseuille flow), and a reactor based on the dispersion model (with the minimum Bodenstein number  $Bo = 50$  applicable to this model). As can be seen, the ideal reactors CSTR and PFTR deviate significantly from the measured curve. Also the dispersion model, based on dispersive turbulent flow in pipes, cannot describe the observed behaviour. The best approximation of the experimental curve via an ideal reactor is obtained with the Poiseuille model. This is reasonable since the parallel channels contribute a main part to the compartment volume, hence influencing strongly the residence time behaviour, and the flow through these channels is laminar. Despite the similarities, the steepness of the Poiseuille curve is considerably higher than that of the measured curve and the experimental curve starts earlier. These facts indicate higher dispersion than in tubes with laminar flow and zones of diminished velocities in the triangular area or bypasses.

In addition, RTD measurements of the inlet and outlet tubes were conducted which are used as input signal for the simulation (see Section 3.2 for a motivation of this approach).

## 3. Numerical simulations

### 3.1. Governing equations

Let  $\tilde{c}$  (mol/m<sup>3</sup>) denote the concentration of eosin in the water. The transport of eosin can be described by a scalar convection–diffusion equation for  $\tilde{c}$ :

$$\frac{\partial \tilde{c}}{\partial t} - D_{ew} \Delta \tilde{c} + \tilde{\mathbf{u}} \cdot \nabla \tilde{c} = 0 \quad \text{in } (0, \tilde{T}] \times \Omega, \quad (1)$$

$$\tilde{c} = \tilde{c}_{in} \quad \text{in } (0, \tilde{T}] \times \Gamma_{in}, \quad (2)$$

$$\frac{\partial \tilde{c}}{\partial \mathbf{n}} = 0 \quad \text{in } (0, \tilde{T}] \times (\Gamma \setminus \Gamma_{in}), \quad (3)$$

$$\tilde{c}(0, \cdot) = 0 \quad \text{in } \Omega. \quad (4)$$

Here,  $\Omega$  is the domain presented in Fig. 5,  $\Gamma$  the boundary of  $\Omega$ ,  $\Gamma_{in}$  the inflow boundary,  $\Gamma_{out}$  the outflow boundary,  $\mathbf{n}$  the outward pointing unit normal vector on  $\Gamma$  and  $\tilde{T} = 3600$  s the final time of the simulation.

We make the simplifying assumption that all physical properties of the mixture concerning molecular transport, especially the coefficient  $D_{ew}$  and the velocity field  $\tilde{\mathbf{u}}$ , are independent of the concentration  $\tilde{c}$ . These assumptions are appropriate for the present situation since we have a laminar flow and the concentration of the additional species (eosin) is so small that it does not significantly alter the physical properties of the background fluid. Then, the velocity field  $\tilde{\mathbf{u}}$  is decoupled from the concentration field.

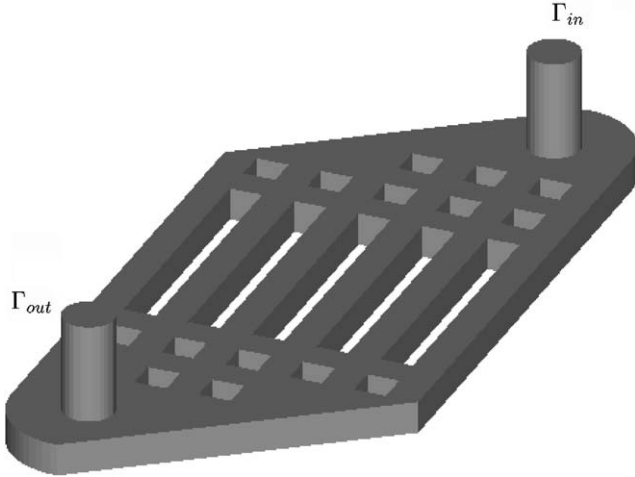


Fig. 5. Fuel cell calculation domain with inflow boundary  $\Gamma_{in}$  and outflow boundary  $\Gamma_{out}$ .

The diffusivity coefficient of eosin in water  $D_{ew}$  was calculated via three methods: (a) Siddiqi and Lucas (1986), (b) Hayduk and Laudie (1974), (c) Wilke and Chang (1955). With an estimation of the molar volume via the group contribution method of Constantinou et al. (1995), the methods resulted in (a)  $D_{ew} = 5.34 \times 10^{-10} \text{ m}^2/\text{s}$  with an error of 13%, (b)  $D_{ew} = 6.41 \times 10^{-10} \text{ m}^2/\text{s}$  with an error of 18% and (c)  $D_{ew} = 6.36 \times 10^{-10} \text{ m}^2/\text{s}$  with an error of 20% (all errors according to Perry and Green, 1997). Due to the larger errors in (b) and (c), we decided to use the diffusivity coefficient of Siddiqi and Lucas, i.e.  $D_{ew} = 5.34 \times 10^{-10} \text{ m}^2/\text{s}$ .

The concentration at the inlet is denoted by  $\tilde{c}_{in}$ . From the experiment, only the mean value

$$\bar{\tilde{c}}_{in}(\tilde{t}) = \frac{\int_{\Gamma_{in}} \tilde{c}_{in}(\tilde{t}, \mathbf{s}) \, ds}{\int_{\Gamma_{in}} ds}$$

is known but not the profile of  $\tilde{c}_{in}$ . We will present in Section 4.2 a numerical study for different inflow profiles  $\tilde{c}_{in}$  which possess the same mean value  $\bar{\tilde{c}}_{in}$ . At the initial time, there is no eosin in  $\Omega$ .

The velocity field  $\tilde{\mathbf{u}}$  in Eq. (1) is given by the flow of the water through the DMFC compartment. This flow is described by the Navier–Stokes equations. Since the steady-state velocity field is much faster established than the steady-state concentration field, the flow is quasi-steady state and hence can be described by the stationary Navier–Stokes equations for incompressible fluids:

$$-v\Delta\tilde{\mathbf{u}} + (\tilde{\mathbf{u}} \cdot \nabla)\tilde{\mathbf{u}} + \frac{\nabla\tilde{p}}{\rho} = \mathbf{0} \quad \text{in } \Omega, \quad (5)$$

$$\nabla \cdot \tilde{\mathbf{u}} = 0 \quad \text{in } \Omega, \quad (6)$$

$$\tilde{\mathbf{u}} = \tilde{\mathbf{u}}_{in} \quad \text{on } \Gamma_{in} \quad (7)$$

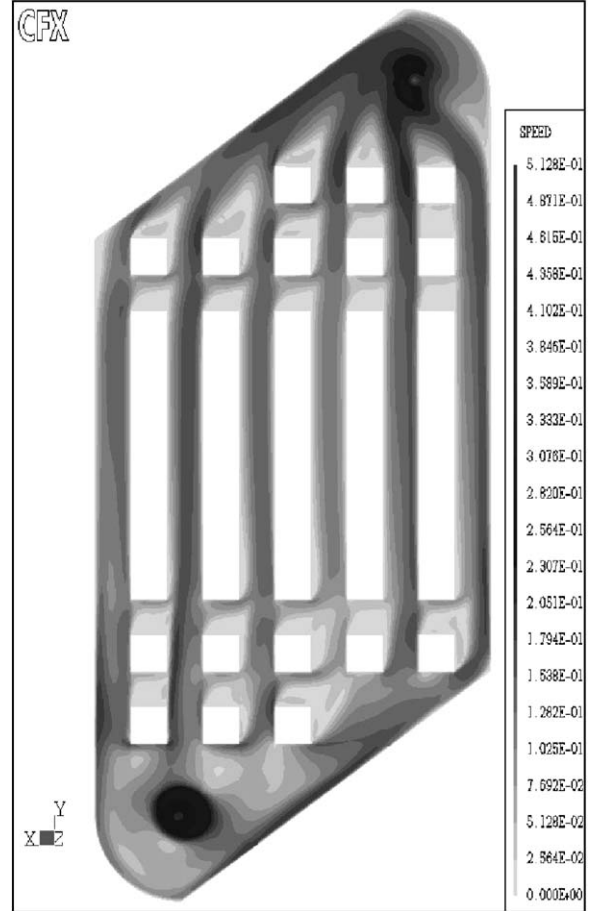


Fig. 6. Velocity field at  $z = 2 \text{ mm}$ .

$$\left( v\nabla\tilde{\mathbf{u}} - \frac{\tilde{p}}{\rho} \mathbb{1} \right) \mathbf{n} = \mathbf{0} \quad \text{on } \Gamma_{out} \quad (8)$$

$$\tilde{\mathbf{u}} = \mathbf{0} \quad \text{on } \Gamma \setminus (\Gamma_{in} \cup \Gamma_{out}). \quad (9)$$

Here,  $\tilde{p}$  ( $\text{kg}/(\text{m s}^2)$ ) is the pressure,  $v = 1.002 \times 10^{-6} \text{ m}^2/\text{s}$  is the kinematic viscosity of water and  $\rho = 998 \text{ kg}/\text{m}^3$  is the density of water, both at 295 K,  $\tilde{\mathbf{u}}_{in}$  the velocity at the inlet and  $\mathbb{1}$  the unit tensor. The velocity field in the cut section  $z = 2 \text{ mm}$  is presented in Fig. 6.

The inflow velocity  $\tilde{\mathbf{u}}_{in}$  is given by  $\tilde{\mathbf{u}}_{in} = (0, 0, (1 - (\tilde{r}/\tilde{r}_0)^2)\tilde{u})$  with  $\tilde{u} = 25/6\pi \text{ mm}/\text{s}$  and the radius of the inflow pipe  $\tilde{r}_0 = 4 \text{ mm}$ . The distance of  $\tilde{\mathbf{x}} \in \Gamma_{in}$  to the centre of the inflow circle is denoted by  $\tilde{r}$ . The inflow profile is a paraboloid and corresponds to the volume flux in the experiment:

$$\begin{aligned} \int_{\Gamma_{in}} \tilde{\mathbf{u}}_{in} \cdot \mathbf{n} \, ds &= \int_0^{2\pi} \int_0^{\tilde{r}_0} (1 - (\tilde{r}/\tilde{r}_0)^2)\tilde{u}\tilde{r} \, d\tilde{r} \, d\phi \\ &= \frac{\pi}{2} \tilde{u}\tilde{r}_0^2 = \frac{100}{3} \text{ mm}^3/\text{s} = 2 \text{ ml}/\text{min}. \end{aligned}$$

The evolution of the averaged outflow of eosin

$$\bar{c}_{\text{out}}(\tilde{t}) = \frac{\int_{\Gamma_{\text{out}}} \tilde{c}(\tilde{t}, \mathbf{s}) \, d\mathbf{s}}{\int_{\Gamma_{\text{out}}} d\mathbf{s}}$$

is the quantity of interest.

The used codes treat dimensionless versions of the governing Eqs. (1)–(9). Taking the characteristic length scale  $L = 1$  mm, the velocity scale  $U = 1$  mm/s, the concentration scale  $5 \times 10^{-6}$  mol/l and the time scale 1 s gives with the usual transformations the dimensionless equations:

$$-Re^{-1} \Delta \mathbf{u} + (\mathbf{u} \cdot \nabla) \mathbf{u} + \nabla p = \mathbf{0} \quad \text{in } \Omega, \quad (10)$$

$$\nabla \cdot \mathbf{u} = 0 \quad \text{in } \Omega, \quad (11)$$

$$\mathbf{u} = \mathbf{u}_{\text{in}} \quad \text{on } \Gamma_{\text{in}}, \quad (12)$$

$$(Re^{-1} \nabla \mathbf{u} - p \mathbb{I}) \mathbf{n} = \mathbf{0} \quad \text{on } \Gamma_{\text{out}}, \quad (13)$$

$$\mathbf{u} = \mathbf{0} \quad \text{on } \Gamma \setminus (\Gamma_{\text{in}} \cup \Gamma_{\text{out}}), \quad (14)$$

$$\frac{\partial c}{\partial t} - \frac{1}{Pe} \Delta c + \mathbf{u} \cdot \nabla c = 0 \quad \text{in } (0, T] \times \Omega, \quad (15)$$

$$c = c_{\text{in}} \quad \text{on } (0, T] \times \Gamma_{\text{in}}, \quad (16)$$

$$\frac{\partial c}{\partial \mathbf{n}} = 0 \quad \text{on } (0, T] \times (\Gamma \setminus \Gamma_{\text{in}}), \quad (17)$$

$$c(0, \cdot) = 0 \quad \text{in } \Omega. \quad (18)$$

The dimensionless quantities are denoted without the tilde. In Eq. (10), the Reynolds number  $Re$  is given by

$$Re = \frac{UL}{\nu} = 0.998$$

and the Peclet number  $Pe$  in Eq. (15) is given by

$$Pe = \frac{LU}{D_{ew}} = 1.87 \times 10^3.$$

The dimensionless inflow velocity is given by

$$\mathbf{u}_{\text{in}} = \frac{\tilde{\mathbf{u}}_{\text{in}}}{U} = \left( 0, 0, \frac{25}{6\pi} \left( 1 - \left( \frac{r}{r_0} \right)^2 \right) \right).$$

### 3.2. Fitting the experimental set-up with the computational domain

The actual experimental set-up for the RTD measurements consists of three parts: the inlet pipe, the anode compartment and the outlet pipe. Inlet and outlet pipe are already volume-minimised connectors from the valve to the compartment and from the compartment to the measuring sensor, respectively, but still they contribute to 36.7% of the whole volume and influence strongly the residence time behaviour of the exemplary anode compartment. To compare the experimental results with the simulations, the influence of inlet and outlet are included in the simulation via the following assumption: we regard the input–output

behaviour of the single setup parts as commutative in terms of concentration and hence assume that the RTD is independent of the arrangement of these parts. This allows to use the connecting pipes' RTD, i.e. the measured concentration signal, as inlet boundary condition of the concentration for the anode compartment.

### 3.3. Finite volume method

Computations with a cell-centred Finite Volume Method (FVM) were carried out with the commercial code CFX 4.4. The discretisation is based on the decomposition of the domain  $\Omega$  into control volumes. The variables are defined at the centre of each control volume. The considered equations are integrated over each control volume, integration by parts is applied, and the arising integrals on the faces of the control volume connect the variables in the centre of the control volume to the variables of their adjacent volumes. For uniform and quasi-uniform meshes, the FVM corresponds to a finite difference scheme of second order.

In our case, a hybrid differencing scheme (HDS) is used to discretise the convective terms in all transport equations. Depending on the size of a local mesh Peclet number, the scheme switches between an upwind differencing (for small mesh Peclet numbers) and a central differencing (for large mesh Peclet numbers) scheme. In this way the needed upwind stabilisation is only used locally in regions where the convection dominates over diffusion. The implicit backward Euler scheme has been used for the time discretisation, which allows larger time steps due to the unconditional stability property.

### 3.4. Finite element method

The simulation with the Finite Element Method (FEM) have been performed with the code MoonNMD, which was developed at the Institut für Analysis und Numerik (John and Matthies, 2003).

#### 3.4.1. The used code MoonNMD

The main features of the research code MoonNMD are:

- Isoparametric finite element discretisations of higher order to adapt curved boundaries sufficiently accurate, see John (2002, 2003b); John and Matthies (2001),
- implicit temporal discretisations,
- efficient iterative solvers for linear systems based on multiple discretisation multilevel approaches, see John (2002); John et al. (2002) for details.

These techniques are considered to be among the most advanced ones in computational fluid dynamics (CFD). The accuracy of the computed results obtained with these approaches has been demonstrated for the Navier–Stokes equations in several numerical studies (John,

2002, 2003b; John and Matthies, 2001). Some of the basic ideas used in the implementation of these algorithms have been described in detail in John (2003a); John and Matthies (2003).

### 3.4.2. Applied discretisations

The Navier–Stokes equations are linearised by a fixed point iteration leading in each iteration step to a linear problem which is usually called Oseen problem. These Oseen problems are discretised by the mapped  $Q_2/P_1^{\text{disc}}$  finite element method. This pair of finite element spaces is one of the most popular ones used for the incompressible Navier–Stokes equations (Fortin, 1993; Gresho and Sani, 2000). It has been analysed in Matthies and Tobiska (2002) and it has been proved to provide very accurate results in computations of characteristic flow parameters like lift and drag coefficients, see John (2002, 2003b); John and Matthies (2001). Using the  $Q_2/P_1^{\text{disc}}$  finite element, the velocity is approximated of second order by a continuous function whereas the discrete pressure is a discontinuous first-order approximation.

The concentration in Eqs. (15)–(18) is approximated by a continuous  $Q_2$  finite element function. Since (15) is an equation with dominating convection, we found it necessary to stabilise the convective term. We used the popular streamline diffusion finite element method (SDFEM), see Hughes and Brooks (1979) or the monograph Roos et al. (1996). A detailed description of the SDFEM for time dependent problems can be found in Codina (1998). The SDFEM involves local parameters  $\delta_K$  which control the amount of additional stabilisation based on the local ratio between diffusion and convection. Let  $h_K$  be the diameter of the mesh cell  $K$ ,  $\|\mathbf{u}(S_K)\|$  be the Euclidean norm of the velocity vector in the barycentre  $S_K$  of  $K$ ,  $Pe_K$  be the local Peclet number  $Pe_K = \|\mathbf{u}(S_K)\| h_K / (2\varepsilon)$  and

$$\alpha = \coth(Pe_K) - \frac{1}{Pe_K}.$$

Similar to Codina (1998), we used the stabilisation parameter

$$\delta_K = \frac{\alpha h_K}{8 \|\mathbf{u}(S_K)\|}.$$

The use of isoparametric finite elements has been proved to be essential for computing accurate results with higher-order finite elements in curved domains, e.g., see John (2002); John and Matthies (2001). That is the reason for using in both equations isoparametric finite elements for the cylindrical pipes to obtain a sufficiently accurate approximation of the curved boundary.

We tested several implicit time stepping schemes for solving (15): the first-order backward Euler scheme, the second-order Crank–Nicolson scheme and the second-order fractional-step  $\theta$ -scheme. In addition, the results obtained with equidistant time steps of several length have been compared.

## 4. Numerical studies and comparison to the experimental results

### 4.1. First-order FVM approach—results for different lengths of the time step

The computational results presented in this section have been obtained with the code CFX 4.4 and the finite volume method described in Section 3.3.

The multi-block grid which has been used in the computations is illustrated in Fig. 7. It includes 37 blocks, 251,056 cells and 297,321 grid points.

In these computations, the experimental mean inflow data has been approximated by a piecewise polynomial (three pieces). This approximation was quite accurate with a mean error of 4%.

We studied the influence of the length of the time step on the evolution of the mean outflow concentration. The results are presented in Fig. 8. It can be observed that the RTDs are very similar for a wide range of time steps. The only small difference is that the outflow of eosin starts somewhat earlier in the computations with large time steps. However, the advantage of using larger time steps is that the overall computing times are considerably reduced.

### 4.2. Second-order FEM approach—results with different inflow profiles $c_{in}$

These studies have been performed with the code MooNMD and the finite element method described in Section 3.4.

The coarsest mesh of the calculations is shown in Fig. 9. The final mesh was obtained from this initial mesh by

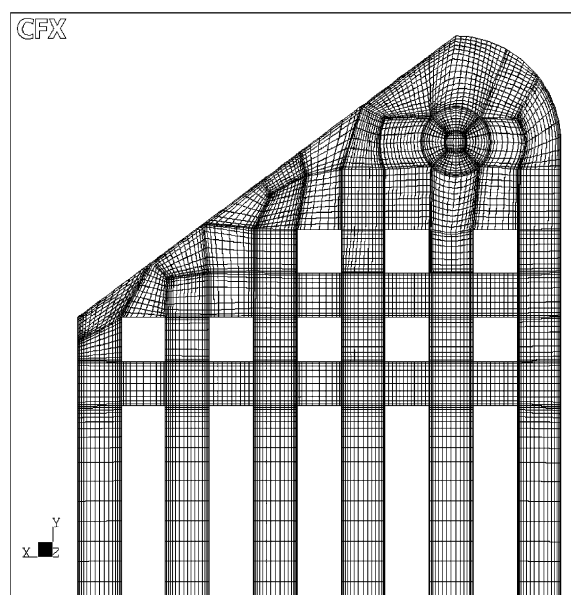


Fig. 7. Grid at  $z = 2$  mm.

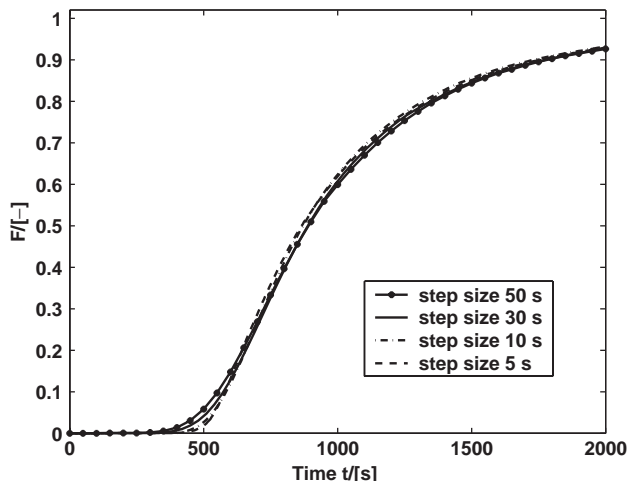


Fig. 8. Comparison of different time steps.

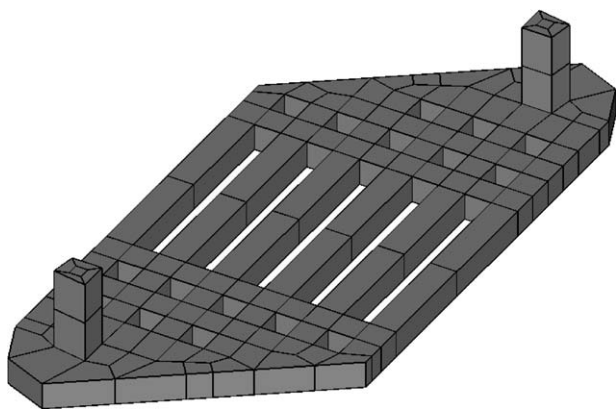


Fig. 9. Coarsest mesh for the numerical studies of Section 4.2.

three refinement steps. In each refinement step, all existing hexahedra are divided into 8 smaller hexahedra, i.e., the number of hexahedral cells is increased by a factor of 8 by one refinement step. Furthermore, during the refinement, the curved boundary was taken into account, i.e., the finer meshes resolve the boundary much better than the shown coarse one.

For approximating each velocity component, we used 641,292 degrees of freedom. This results in a total number of 1,923,876 degrees of freedom for the velocity vector field. The scalar pressure function was calculated by using 294,912 unknowns. Finally, the concentration in the fuel cell was approximated by 641,292 degrees of freedom.

We found in our numerical studies that the averaged concentration at the outflow  $\bar{c}_{\text{out}}(t)$  shows a very small dependence on the time discretisation scheme and the length of the time step. In these studies, we tested time step lengths  $\Delta t \in [0.01, 20]$ . For a given length of the time step, all considered implicit time stepping schemes obtained almost the same results for  $\bar{c}_{\text{out}}(t)$ . In the following, we

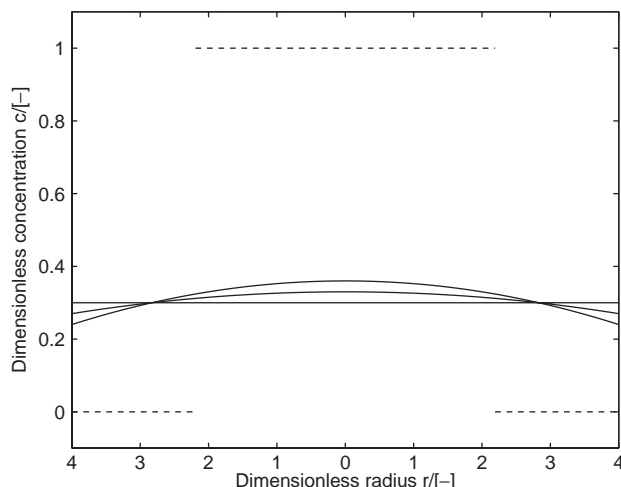


Fig. 10. Radial cut of different concentration distributions at  $\Gamma_{\text{in}}$  with the same average 30% of maximum concentration.

present results obtained with the Crank–Nicolson scheme and  $\Delta t = 10$ .

We will present a numerical study of the influence of the chosen concentration profile  $c_{\text{in}}(t, r)$  on the averaged outflow  $\bar{c}_{\text{out}}(t)$ . All considered inflow profiles have the same average  $\bar{c}_{\text{in}}(t)$ . Fig. 10 shows four different inflow profiles in a radial cut such that in all cases the averaged concentration is 30% of the maximal concentration.

The three solid curves in Fig. 10 are of the form

$$c_{\text{in}}(t, r) = \bar{c}(t)(a - br^2),$$

where  $a, b$  are constants in space and  $r$  is the distance of a point to the axis of the inflow pipe. The dashed curve is given by

$$c_{\text{in}}(t, r) = \begin{cases} 1, & r < r_1(t), \\ 0, & r_1(t) \leq r \leq r_0, \end{cases}$$

where  $r_1$  is chosen such that the averaged concentration corresponds to a given value. In the example with 30% of the maximal concentration, there is  $r_1 = 0.4\sqrt{30}$ . In the course of the time,  $r_1$  tends to  $r_0$ .

Fig. 11 shows the averaged concentration  $\bar{c}_{\text{out}}(t)$  at the outflow boundary  $\Gamma_{\text{out}}$  for the four different local concentration distribution at  $\Gamma_{\text{in}}$  together with the outflow concentration obtained by the experiment. The curve from the experiment shows a steeper increase than all numerical simulations. We see that there are also differences between the calculations for the different local concentration distributions. These differences become more obvious in Fig. 12. In this figure, the differences of the numerical results to the experimental output  $\bar{c}_{\text{out,exp}}(t)$  are presented. In order to get smooth curves, the experimental data were smoothed by using a cubic spline interpolation. The mean quadratic

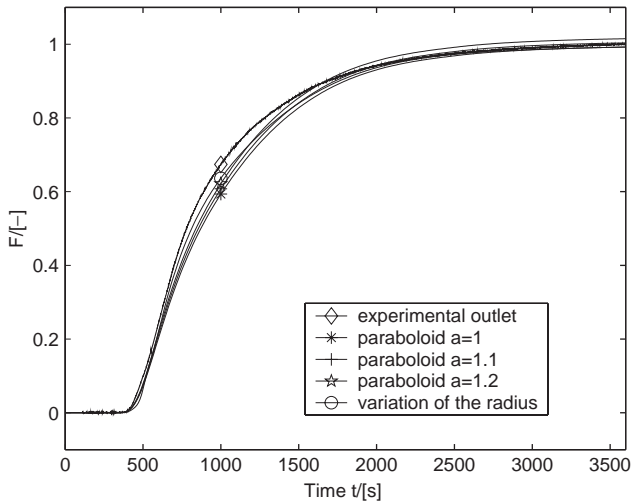


Fig. 11. Simulated RTDs for various inlet concentration profiles vs. experimental RTD.

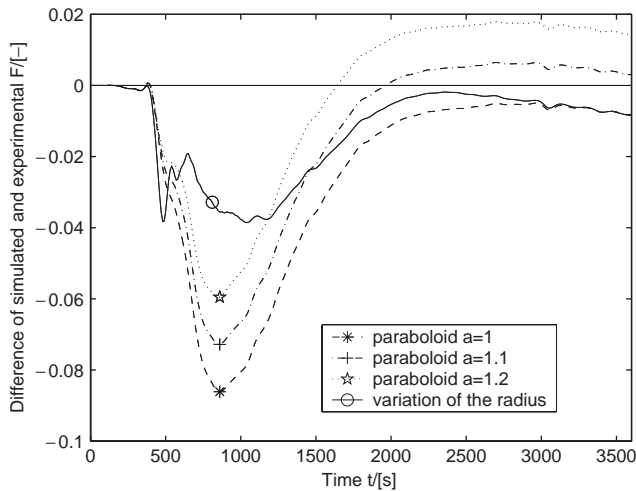


Fig. 12. Differences of averaged concentration at the outflow boundary  $F_{out}$  with respect to experimental data.

Table 2  
Error in the quadratic mean

|            | $a = 1.0$   | $a = 1.1$   | $a = 1.2$   | Radius      |
|------------|-------------|-------------|-------------|-------------|
| Mean error | $3.54e - 2$ | $2.83e - 2$ | $2.42e - 2$ | $1.83e - 2$ |

error

$$\left( \sum_{k=0}^{360} |\bar{c}_{out,exp}(k\Delta t) - \bar{c}_{out,num}(k\Delta t)|^2 \right)^{1/2} / \sqrt{361}$$

using the values at the discrete times  $0, \Delta t, 2\Delta t, \dots$  with  $\Delta t = 10$  is given in Table 2. It reveals that there is a small error between experiment and numerical simulations ( $< 4\%$ ) for all inlet profiles. The best agreement

with the experimental data has been obtained by using the inflow profile where the radius  $r_1(t)$  varies. The use of the constant inflow profile gives the largest error.

#### 4.3. Concentration distribution in the cell

The transport of eosin through the anode compartment was recorded by a video camera. The colour intensity represents the local mean concentration over the depth of the cell. Subsequently, the video was digitally post-processed by assigning different colour intensities, i.e. concentrations, to different colours. From some snapshots, shown in Figs. 13(a)–(c), it can be observed that the concentration fronts propagate temporally shifted, i.e. asynchronously, through the channels. The front propagating through the third channel (from the right) is fastest, followed by the fronts of the neighbouring channels. The concentration in the channel farthest away from the inlet is increasing significantly later. During dynamic feed operation of fuel cells using this flow bed design, the regions with slower fuel propagation will, due to lower conversion rates, be less efficient for current production. In addition, a non-ideal tracer distribution and mixing behaviour in the triangular areas is visible. Bypasses and dead zones can be noticed, validating the previous interpretation of the residence time curve (Section 2.3).

Fig. 13 presents, besides the experimental snapshots (a)–(c), snapshots of the CFX simulation (d)–(f). These show the eosin concentration distribution vs. time in the middle cut (depth  $z = 0.5 z_{max}$ ). Pictures of the FEM simulation correlate to these, but are not presented here. Although the simulated pictures are not directly comparable by time scale to the experimental snapshots (see Section 3.2), they show qualitatively a remarkably strong similarity to these. Figs. 13(a) and (d) show the concentration distribution at the beginning. Except for smaller regions, the triangular area shows a concentration of at least 50% of the maximum concentration  $c_{max}$  and the CFX concentration distribution matches the one of the experiment. The same can be said for Figs. 13(b) and (e), and (c) and (f), respectively. Nonetheless, a small deviation can be found: in the experiment the eosin propagation through channel three, counted from the right side, is slightly faster than in channel two, which is vice versa in the simulation.

#### 4.4. Comparison of the results obtained with CFX 4.4 and MoonMD

A comparison of the experimental RTD to the best results computed with the codes CFX 4.4 and MoonMD is presented in Fig. 14. It can be seen that on the one hand the numerical results are in good agreement with the experimental one. But on the other hand, also some differences between the computed RTDs can be observed. The RTD computed with MoonMD is closer to the experimental RTD from the

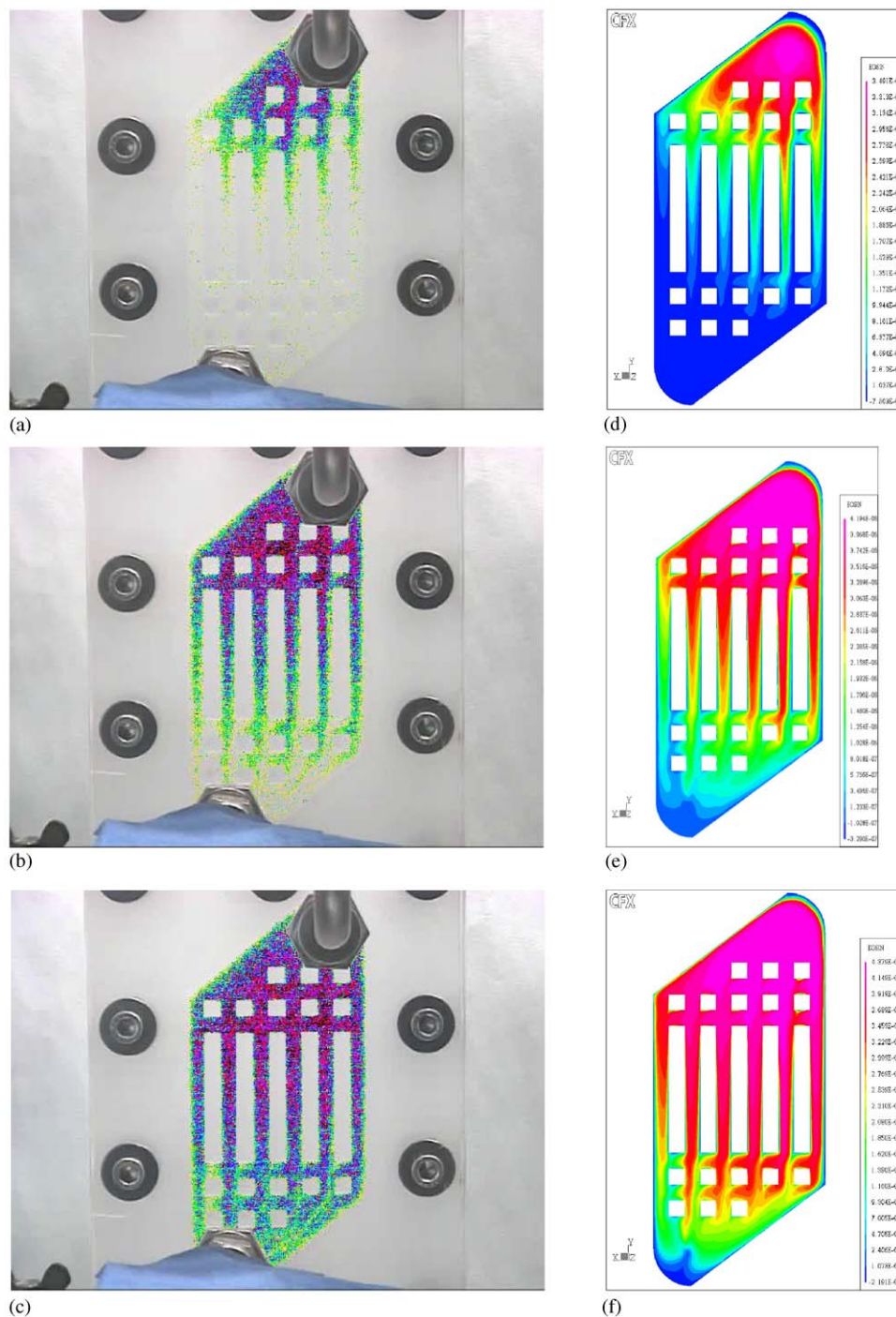


Fig. 13. Qualitative comparison of an experimental video (a,b,c) and a CFX simulation (d,e,f).

starting of the outflow of eosin at around 400 s to around 1000 s. In the time interval from 1100 to 1800 s, the RTD computed with CFX 4.4 matches better to the experimental one. The error in the quadratic mean of these curves is 1.83% for MoonMD and 4.55% for CFX 4.4. This shows that the differences are small. Altogether, both codes are able to simulate the RTD of the rhomboidal anode compartment with a good accuracy.

## 5. Conclusions

The direction of the research work presented in this paper is the characterisation and improvement of the performance of DMFC anode compartments. A simplified parallel flow bed with triangular inlet and outlet zones was designed and constructed. 3D CFD methods as well as experimental methods were applied to analyse the RTD.

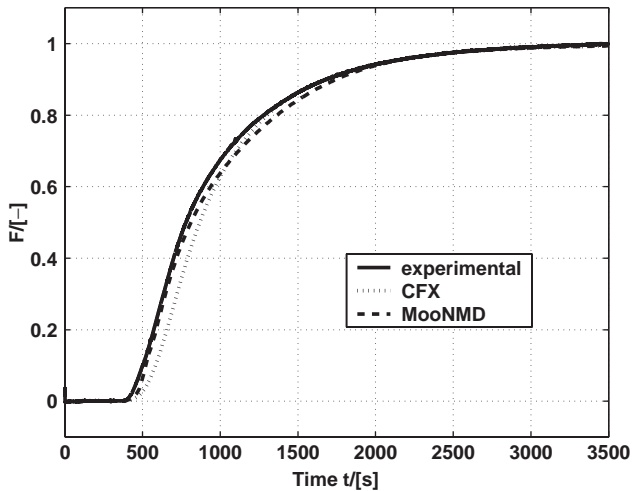


Fig. 14. RTDs of the experiment and the numerical simulations.

The cell's residence time behaviour can be approximated as the residence time behaviour of a laminar tube with convective and dispersive transport. Simulated results could be compared to experimental results via assuming that the experimental RTD of the inlet and outlet pipes can be used as input signal for the CFD simulations. RTDs computed with the codes CFX 4.4 and MooNMD were in good agreement with experimental measurements. In addition, the reliability of the numerical simulations was proved by showing that the computed RTDs depend only slightly on the type of discretisation in space (finite volume or finite element method), the time stepping schemes, the length of the time step and the inflow profile for the concentration.

A study of the fuel distribution in the active area showed concentration fronts propagating temporally shifted, i.e. asynchronously, through the channels. Channels where the concentration front arrived delayed will lead to smaller local current densities under dynamic fuel cell operation. In addition, small dead zones in the triangular regions could be observed.

The presented analysis of the RTDs and concentration distributions provided evidence of weaknesses of the simplified rhomboidal flow bed design. None-the-less, in this study the design is not chosen due to its optimum performance, but to have a basic geometry suitable for RTD and CFD simulations. This approach proved reasonable. The geometry may be enhanced by refining the channel sizes and the distribution elements in the triangular zones. In addition, a further option is to increase the low ratio between active and geometric area caused by the triangular zones. This is done either by minimising the triangular area or by considering alternative flow fields without such distributors, e.g. parallel channel design or spot design. Such studies are subject of our current research activities.

## Notation

|  |  |
|--|--|
| $Bo$                                       | Bodenzahl number, dimensionless  |
| $\tilde{c}, c$                             | concentration, mol/m <sup>3</sup> ; dimensionless concentration, dimensionless                 |
| $\tilde{c}_{in}, c_{in}$                   | inflow concentration mol/m <sup>3</sup> ; dimensionless inflow concentration, dimensionless    |
| $\bar{\tilde{c}}_{in}, \bar{c}_{in}$       | mean values of $\tilde{c}_{in}$ and $c_{in}$   |
| $\tilde{c}_{out}, c_{out}$                 | outflow concentration, mol/m <sup>3</sup> , dimensionless outflow concentration, dimensionless |
| $\bar{\tilde{c}}_{out}, \bar{c}_{out}$     | mean values of $\tilde{c}_{out}$ and $c_{out}$   |
| $D_{ew}$                                   | diffusion coefficient of eosin in water, m <sup>2</sup> /s                                     |
| $F$  | cumulative residence time, dimensionless   |
| $L$  | characteristic length scale, 1 mm  |
| $\tilde{p}, p$                             | pressure kg/(m s <sup>2</sup> ); dimensionless pressure, dimensionless                         |
| $Pe$                                       | Peclet number, dimensionless   |
| $\tilde{r}_0$                              | radius of the inlet and outlet pipes, 4 mm   |
| $Re$                                       | Reynolds number, dimensionless   |
| $t$  | time, s  |
| $T$  | final time, s  |
| $\tilde{\mathbf{u}}, \mathbf{u}$           | velocity, m/s; dimensionless velocity, dimensionless   |
| $\tilde{\mathbf{u}}_{in}, \mathbf{u}_{in}$ | velocity at the inlet, m/s; dimensionless velocity at the inlet, dimensionless                 |
| $U$  | characteristic velocity scale, 1 mm/s  |
| $V$  | cell volume, ml  |
| $V_F$                                      | volume flow, ml/min  |

## Greek letters

|                             |  |
|-----------------------------|--|
| $\Gamma$                    | boundary of $\Omega$                           |
| $\Gamma_{in}, \Gamma_{out}$ | boundary at the inlet and outlet, respectively |
| $\Delta t$                  | length of the time step                        |
| $\theta$                    | dimensionless time, dimensionless              |
| $\nu$                       | kinematic viscosity, m <sup>2</sup> /s         |
| $\rho$                      | density, kg/m <sup>3</sup>                     |
| $\tau$                      | mean residence time, s                         |
| $\Omega$                    | domain of the anode compartment                |

## Acknowledgements

R. Lübke was supported under grant FOR 468 by the Deutsche Forschungsgemeinschaft (DFG).

## References

- Amphlett, J., Peppley, B., Halliop, E., Sadiq, A., 2001. The effect of anode flow characteristics and temperature on the performance of a direct methanol fuel cell. *Journal of Power Sources* 96, 204–213.
- Argyropoulos, P., Scott, K., Taama, W., 1999a. Carbon dioxide evolution patterns in direct methanol fuel cells. *Electrochimica Acta* 44, 3575–3584.
- Argyropoulos, P., Taama, W., Scott, K., 1999b. Engineering & Modelling of Large Scale Liquid fed Direct Methanol Fuel Cells Stacks. *Symposium Series*, Vol. 145, Icheme.

- Arico, A., Creti, P., Baglio, V., Modica, E., Antonucci, V., 2000. Influence of flow design on the performance of a direct methanol fuel cell. *Journal of Power Sources* 91, 202–209.
- Arico, A., Srinivasan, S., Antonucci, V., 2001. DMFCs: from fundamental aspects to technology development. *Fuel Cells* 1 (2), 133–161.
- Baxter, S., Battaglia, V., White, R., 1999. Methanol fuel cell model: anode. *Journal of the Electrochemical Society* 146, 437–447.
- Codina, R., 1998. Comparison of some finite element methods for solving the diffusion–convection–reaction equation. *Computer Methods in Applied Mechanics and Engineering* 156, 185–210.
- Constantinou, L., Gani, R., O’Connell, J., 1995. Estimation of the acentric factor and the liquid molar volume at 298 K using a new group contribution method. *Fluid Phase Equilibria* 103, 11–22.
- Dutta, S., Shimpalee, S., Zee, J.V., 2000. Three-dimensional numerical simulation of straight channel pem fuel cells. *Journal of Applied Electrochemistry* 30, 135–146.
- Fortin, M., 1993. Finite element solution of the Navier–Stokes equations. In: Iserles, A. (Ed.), *Acta Numerica*. Cambridge University Press, Cambridge, pp. 239–284.
- Geiger, A., Lehmann, E., Vontobel, P., Scherer, G., 2000. Direct methanol fuel cell—in situ investigation of carbon dioxide patterns in anode flow fields by neutron radiography. PSI Scientific Report, General Energy, Paul Scherrer Institut, Villigen, Switzerland, pp. 86–87.
- Geiger, A., Rager, T., Scherer, G., Wokaun, A., 2001. Novel membranes for application in direct methanol fuel cells. PSI Scientific Report, General Energy, Paul Scherrer Institut, Villigen, Switzerland, pp. 99–100.
- Gresho, P., Sani, R., 2000. *Incompressible Flow and the Finite Element Method*. Wiley, Berlin.
- Gulzow, E., Kaz, T., Reissner, R., Sander, H., Schilling, L., Bradke, M., 2002. Study of membrane electrode assemblies for direct methanol fuel cells. *Journal of Power Sources* 105, 261–266.
- Hayduk, W., Laudie, H., 1974. Prediction of diffusion coefficients for nonelectrolytes in dilute aqueous-solutions. *A.I.Ch.E. Journal* 20 (3), 611–615.
- He, W., Chen, Q., 1998. Three-dimensional simulation of a molten carbonate fuel cell stack under transient conditions. *Journal of Power Sources* 73, 182–192.
- Heinzel, A., Barragan, V.M., 1999. A review of the state-of-the-art of the methanol crossover in direct methanol fuel cells. *Journal of Power Sources* 84 (1), 70–74.
- Hikita, S., Yamane, K., Nakajima, Y., 2002. Influence of cell pressure and amount of electrode catalyst in MEA on methanol crossover of direct methanol fuel cell. *JSAE Review* 23 (1), 133–135.
- Hughes, T., Brooks, A., 1979. A multidimensional upwind scheme with no crosswind diffusion. In: Hughes, T. (Ed.), *Finite Element Methods for Convection Dominated Flows*, AMD, Vol. 34. ASME, New York, pp. 19–35.
- John, V., 2002. Higher order finite element methods and multigrid solvers in a benchmark problem for the 3D Navier–Stokes equations. *International Journal for Numerical Methods in Fluids* 40, 775–798.
- John, V., 2003a. Large eddy simulation of turbulent incompressible flows. Analytical and numerical results for a class of LES Models. *Lecture Notes in Computational Science and Engineering* 34, Springer Verlag, Berlin, Heidelberg, New York.
- John, V., 2003b. Reference values for drag and lift of a two-dimensional time dependent flow around a cylinder, submitted for publication.
- John, V., Matthies, G., 2001. Higher order finite element discretizations in a benchmark problem for incompressible flows. *International Journal for Numerical Methods in Fluids* 37, 885–903.
- John, V., Matthies, G., 2003. MoonNMD—a program package based on mapped finite element methods. *Computing and Visualization in Science*, accepted for publication.
- John, V., Knobloch, P., Matthies, G., Tobiska, L., 2002. Non-nested multi-level solvers for finite element discretizations of mixed problems. *Computing* 68, 313–341.
- Jorissen, L., Gogel, V., Kerres, J., Garche, J., 2002. New membranes for direct methanol fuel cells. *Journal of Power Sources* 105, 267–273.
- Kulikovsky, A., Divisek, J., Kornyshev, A., 2000. Two-dimensional simulation of direct methanol fuel cell a new (embedded) type of current collector. *Journal of the Electrochemical Society* 147 (3), 953–959.
- Lavric, I., Staiti, P., Novak, P., Hocevar, S., 2001. Computational fluid dynamics study of phosphotungstic acid electrolyte-based fuel cell (PWAFc). *Journal of Power Sources* 96, 303–320.
- Matthies, G., Tobiska, L., 2002. The inf–sup condition for the mapped  $Q_k/P_{k-1}^{disc}$  element in arbitrary space dimensions. *Computing* 69, 119–139.
- Nordlund, J., Roessler, A., Lindbergh, G., 2002. The influence of electrode morphology on the performance of a DMFC anode. *Journal of Applied Electrochemistry* 32, 259–265.
- Perry, R., Green, D., 1997. *Perry’s Chemical Engineers’ Handbook*, 7th Edition. McGraw-Hill, New York.
- Roos, H.-G., Stynes, M., Tobiska, L., 1996. *Numerical Methods for Singularly Perturbed Differential Equations*. Springer, Berlin.
- Schultz, T., Zhou, S., Sundmacher, K., 2001. Current status of and recent developments in the direct methanol fuel cell. *Chemical Engineering Technology* 24 (12), 1223–1233.
- Scott, K., Taama, W., Argyropoulos, P., 1998. Material aspects of the liquid feed direct methanol fuel cell. *Journal of Applied Electrochemistry* 28, 1389–1397.
- Scott, K., Taama, W., Argyropoulos, P., 1999a. Engineering aspects of the direct methanol fuel cell system. *Journal of Power Sources* 79, 43–59.
- Scott, K., Taama, W., Argyropoulos, P., Sundmacher, K., 1999b. The impact of mass transport and methanol crossover on the direct methanol fuel cell. *Journal of Power Source* 83, 204–216.
- Scott, K., Taama, W., Kramer, S., Argyropoulos, P., Sundmacher, K., 1999c. Limiting current behaviour of the direct methanol fuel cell. *Electrochimica Acta* 45, 945–957.
- Scott, K., Argyropoulos, P., Yiannopoulos, P., Taama, W., 2001. Electrochemical and gas evolution characteristics of direct methanol fuel cells with stainless steel mesh flow beds. *Journal of Applied Electrochemistry* 31, 823–832.
- Shukla, A., Jackson, C., Scott, K., Raman, R., 2002. An improved-performance liquid-feed solid-polymer-electrolyte direct methanol fuel cell operating at near-ambient conditions. *Electrochimica Acta* 47, 3401–3407.
- Siddiqi, M., Lucas, K., 1986. Correlations for prediction of diffusion in liquids. *Canadian Journal of Chemical Engineering* 64 (5), 839–843.
- Sundmacher, K., Scott, K., 1999. Direct methanol polymer electrolyte fuel cell: analysis of charge and mass transfer in the vapour–liquid–solid system. *Chemical Engineering Science* 54, 2927–2936.
- Sundmacher, K., Schultz, T., Zhou, S., Scott, K., Ginkel, M., Gilles, E., 2001. Dynamics of the direct methanol fuel cell (DMFC): experiments and model-based analysis. *Chemical Engineering Science* 56, 333–341.
- Wang, J., Wasmus, S., Savinell, R., 1996. Real-time mass spectrometric study of the methanol crossover in a direct methanol fuel cell. *Journal of the Electrochemical Society* 143, 1233–1239.
- Wei, Z., Wang, S., Yi, B., Liu, J., Chen, L., Zhou, W., Li, W., Xin, Q., 2002. Influence of electrode structure on the performance of a direct methanol fuel cell. *Journal of Power Sources* 106, 364–369.
- Wilke, C., Chang, P., 1955. Correlation of diffusion coefficients in dilute solutions. *A.I.Ch.E. Journal* 1 (2), 264–270.
- Zhou, S., Schultz, T., Peglow, M., Sundmacher, K., 2001. Analysis of the nonlinear dynamics of a direct methanol fuel cell. *Physical Chemistry Chemical Physics* 3, 347–355.